

*Review*

# The structure, dynamics, and energetics of protein adsorption – lessons learned from adsorption of statherin to hydroxyapatite

Gil Goobes,<sup>1\*§</sup> Rivka Goobes,<sup>2</sup> Wendy J. Shaw,<sup>1#</sup> James M. Gibson,<sup>2†</sup> Joanna R. Long,<sup>2‡</sup> Vinodkumar Raghunathan,<sup>1</sup> Ora Schueler-Furman,<sup>3††</sup> Jennifer M. Popham,<sup>1</sup> David Baker,<sup>3</sup> Charles T. Campbell,<sup>1</sup> Patrick S. Stayton<sup>2</sup> and Gary P. Drobny<sup>1\*</sup>

<sup>1</sup> Department of Chemistry, University of Washington, Seattle WA 98195, USA

<sup>2</sup> Department of Bioengineering, University of Washington, Seattle WA 98195, USA

<sup>3</sup> Department of Biochemistry, University of Washington, Seattle WA 98195, USA

Received 23 July 2007; Revised 27 September 2007; Accepted 1 October 2007

Proteins are found to be involved in interaction with solid surfaces in numerous natural events. Acidic proteins that adsorb to crystal faces of a biomineral to control the growth and morphology of hard tissue are only one example. Deducing the mechanisms of surface recognition exercised by proteins has implications to osteogenesis, pathological calcification and other proteins functions at their adsorbed state. Statherin is an enamel pellicle protein that inhibits hydroxyapatite nucleation and growth, lubricates the enamel surface, and is recognized by oral bacteria in periodontal diseases. Here, we highlight some of the insights we obtained recently using both thermodynamic and solid state NMR measurements to the adsorption process of statherin to hydroxyapatite. We combine macroscopic energy characterization with microscopic structural findings to present our views of protein adsorption mechanisms and the structural changes accompanying it and discuss the implications of these studies to understanding the functions of the protein adsorbed to the enamel surfaces. Copyright © 2007 John Wiley & Sons, Ltd.

**KEYWORDS:** solid-state NMR; protein; structure; adsorption; recoupling; magic angle spinning; calorimetry

## INTRODUCTION TO BIOMINERALIZATION AND BACTERIAL ADHESION TO MINERALIZED TISSUE

Elaborate mechanisms are used by living organisms to form organic–inorganic composites in hard tissues through the interaction of proteins, and ultimately cells, with inorganic mineral phases. The enhanced mechanical properties of biocomposites such as bone and teeth thus result from the

operation of proteins that regulate osteogenesis microscopically at the organic–inorganic interface. The underlying molecular mechanisms of biomineralization regulation are of major importance to dentistry and medicine, as impairment of biomineralization processes can lead to osteoporosis, dental calculus, arthritis, and pathological mineralization of the form observed in atherosclerotic plaque, artificial heart valve calcification, and kidney stone.<sup>1–3</sup> A better understanding of the biomolecular mechanisms used to promote or slow down crystal growth could provide important design principles for the development of mineralization promoters or blockers in dentistry, orthopedics, urology, and cardiology. Similarly, insights into how these proteins recognize and assemble in bioactive form on inorganic mineral phases could also aid in the development of better surface coatings providing enhanced biocompatibility of implantable devices and for hard tissue engineering and regeneration technologies.

Understanding the function of any protein requires that the structure of the molecule be defined within its biological environment; in this case, the fold of a biomineralization protein in contact with the crystal surface of the mineral. In addition, the precise nature of the interactions between the protein and the crystal which underlie the recognition

\*Correspondence to: Gil Goobes and Gary P. Drobny, Department of Chemistry, University of Washington, Box 351700, Seattle WA 98195, USA. E-mail: Gil.Goobes@mail.biu.ac.il; drobny@chem.washington.edu

§Current address: Department of Chemistry, Bar Ilan University, Ramat Gan 52900, Israel.

#Current address: Pacific Northwest National Laboratory, Richland, WA 99352, USA.

†Current address: Department of Chemistry and Chemical Biology, Rensselaer Polytechnic Institute, Troy, NY 12180, USA.

‡Current address: Department of Biochemistry and Molecular Biology, McKnight Brain Institute, University of Florida, Gainesville, FL 32610, USA.

††Current address: Department of Molecular Genetics and Biotechnology, Hebrew University, Hadassah Medical School, Jerusalem 91120, Israel.

process must be understood. This requires knowledge of the contacts formed between amino acid side chains and ions in the crystal faces and contributions of water molecules to these interactions.

The biological context, in which the protein functions, includes not only the mineralized tissue surface but also other proteins, glycoproteins, cells, and pathogens that it interacts with. For an oral cavity protein like statherin, the tooth enamel pellicle constituents as well as microbial cells serve as its biological microenvironment. These microbial cells, which adhere to the surface of the tooth, colonize and develop into films that are central to oral cavity diseases from gingivitis to periodontitis. Their attachment is currently conceived to be through binding to statherin and other proteins adsorbed to enamel and other oral cavity surfaces. Several works have shown that statherin and proline-rich proteins (PRPs) adsorbed to hydroxyapatite (HAP) serve as receptors for adhesion of colonizing bacteria to enamel surfaces. These salivary proteins are recognized by fimbriae, antennae systems in the microorganism cells, solely when adsorbed to HAP and show no binding capabilities to the free protein. The binding sites in both statherin and fimbriillin, the monomeric unit of these antennae systems, were identified later on.

Investigations of protein–mineral interactions are typically carried out using techniques that characterize macroscopic quantities of the protein's adsorption to the mineral crystals. Equilibrium properties such as protein–crystal binding constants are derived from adsorption isotherm (AI) measurements, and kinetic parameters comparing the crystal growth rate in the presence and absence of the protein adsorbed are obtained from constant composition kinetics measurements.<sup>4,5</sup> In addition, binding enthalpies and affinities for proteins to mineral surfaces can be derived from isothermal titration calorimetry (ITC) measurements, as we have recently shown.<sup>6,7</sup> When observations from the two techniques are merged, remarkable insights can be obtained about the driving forces for adsorption and the different mechanisms of binding to the surface. These techniques can help identify residues in the protein that are involved in interaction with the mineral surface indirectly by mutagenesis work;<sup>7</sup> however, to probe the actual interaction interface directly, one must utilize microscopic techniques.

High-resolution spectroscopic methods provide detailed information about the atomic level structure of the protein on the crystal faces, under physical conditions that are biologically relevant. Invaluable information about the secondary structural motifs and tertiary folding that characterize the adsorbed protein, together with information on the interaction of protein side chains with atoms on the crystal face, may lead to an understanding of how particular proteins promote or inhibit nucleation. Molecular level structure information for proteins that interact with crystals<sup>8</sup> and proteins that directly control calcification processes<sup>9</sup> in hard tissue is very scarce. Basic questions about how the proteins attach to the crystal surfaces and whether acidic residues are directly involved in binding to calcium phosphate surfaces remain largely unanswered at the fundamental molecular level. In

order to develop a better structure–function level understanding of the protein–crystal molecular recognition, we have begun to utilize solid-state NMR techniques to determine the structure of proteins and peptides on HAP surfaces and captured along the way interesting molecular dynamics information for the proteins on the biomineral surface.

Solid-state NMR spectroscopy is the method of choice to investigate protein structure at biomaterial interfaces, despite the complex nature of the protein surface problem. Structural determination that includes defining the secondary and tertiary structures of the adsorbed protein and by implication of any structural changes that occur upon binding to the surface can be approached using this spectroscopic method. Concurrently, the chemical composition and structure at the interface of the protein side chains and the crystal surface can be deduced. Motional features of the adsorbed protein that are observable under NMR time scale can also be detected. Measurements in these systems are carried out under hydrated conditions in a buffer that partially simulates ion concentration in saliva and pellicle environments.

Principal information regarding adsorption characteristics of proteins on surfaces can be inferred from a combined approach that utilizes microscopic high-resolution measurements and macroscopic thermodynamic characterization that provide information about the binding mechanisms of protein molecules to the surface. For statherin adsorption to HAP, we found that complementary insights from solid-state NMR measurements and from ITC and adsorption isotherms provided further insights into the structure of the active protein, the underlying mechanisms of adsorption and the relation between structures in the bound adsorbed state, and the different functions that statherin carries in the oral cavity.

In this review, we highlight recent work that provides insights into the structure–function relationships of the protein in contact with the mineral crystal and with bacterial cells that employ it as a means of adhering to enamel surfaces. This work also provides guidelines for studying other protein–crystal systems in molecular detail.

## BIOPHYSICAL METHODS FOR THE STUDY OF PROTEIN ADSORPTION THERMODYNAMICS ONTO CRYSTALLINE MINERAL SURFACES

Protein adsorption mechanisms onto surfaces have been explored by calorimetry in the field of chromatography, studying adsorption of proteins to support materials and in the field of biomaterial research, investigating the adsorption of proteins onto surfaces of polymers and colloids.<sup>10–14</sup> Thermodynamic characterization can provide mechanistic insights into the basis of protein function. The free energy of adsorption is derived from equilibrium-binding isotherm analysis after adopting model assumptions. Independent measurement of the adsorption enthalpy through calorimetric techniques permits separable quantification of enthalpic and entropic contributions to the free energy change, thus providing us with better comprehension of the mechanistic aspects of adsorption.<sup>6</sup>

### Isothermal titration calorimetry

In order to adapt ITC to measurements of proteins adsorbed to surfaces, we revisited the basic equations that describe the heat exchange during titration of protein aliquots into a cell containing crystalline mineral with predetermined surface area in a recent publication.<sup>6</sup> We have outlined the necessary modifications to the ITC equations that describe the titration curve and the approach to normalizing the surface area and expressed it in terms of the effective concentration of surface sites available for protein binding. In equilibrium, the adsorption constant,  $K_{\text{ads}}$ , is given by

$$K_{\text{ads}} = \frac{\theta}{(1 - \theta)[C]} \quad (1)$$

where  $\theta$  is the fractional coverage and  $[C]$  is the concentration of free protein. This concentration is related to the total concentration of the protein through

$$[C] = C_t - \theta M_t' \quad (2)$$

where the product  $\theta M_t'$  describes the concentration of adsorbed protein in equilibrium. The quantity  $M_t'$  describes the molar concentration of adsorption sites on the surface per unit volume in the ITC cell and in general is not readily known since a binding site for a particular protein molecule is not easy to define. We proposed using the information obtained from the independent AI measurements of statherin to HAP and Brunauer, Emmett, and Teller (BET) measurements of the mineral surface area in order to calculate  $M_t'$ . This quantity is obtained by multiplying  $N_{\text{max}}$ , the maximum number of sites accessible to the protein on the HAP surface, by the surface area (SA) of HAP and by the density of HAP in the suspension inserted into the ITC cell as follows:

$$M_t' = N_{\text{max}} \left[ \frac{\text{moles}}{\text{m}^2} \right] \times \text{SA} \left[ \frac{\text{m}^2}{\text{gr}} \right] \times D \left[ \frac{\text{gr}}{\text{L}} \right]. \quad (3)$$

This approach to calculating  $M_t'$  relies on the BET technique to define the total surface area and can be limited by accessibility differences of surface sites to protein molecules *versus* small molecules in gaseous phase actually used in the BET experiment. Rearranging the equilibrium constant equation to the following form:

$$\theta = \frac{K_{\text{ads}}[C]}{1 + K_{\text{ads}}[C]} \quad (4)$$

and plugging Eqns (2) and (3) into it, the fractional coverage  $\theta$  attains a quadratic form

$$\theta^2 - \theta \left[ 1 + \frac{C_t}{M_t'} + \frac{1}{K_{\text{ads}}M_t'} \right] + \frac{C_t}{M_t'} = 0 \quad (5)$$

which can be solved in terms of the total concentration of protein  $C_t$ , the total concentration of adsorption sites  $M_t'$ , and the adsorption equilibrium constant  $K_{\text{ads}}$ .

The total measured heat content of the solution in the ITC cell is then given by

$$Q = \theta M_t' \Delta H V_0 = \frac{M_t' \Delta H V_0}{2} \left[ 1 + \frac{C_t}{M_t'} + \frac{1}{K_{\text{ads}}M_t'} - \sqrt{\left( 1 + \frac{C_t}{M_t'} + \frac{1}{K_{\text{ads}}M_t'} \right)^2 - \frac{4C_t}{M_t'}} \right] \quad (6)$$

where  $V_0$  is the working ITC cell volume and  $\Delta H$  is the enthalpy change during the adsorption reaction. The titration curve is obtained from the differential heat content between injection  $i - 1$  and  $i$  using the following expression:

$$\Delta Q(i) = Q(i) - Q(i - 1) + \frac{dV_i}{V_0} \left[ \frac{Q(i) + Q(i - 1)}{2} \right] \quad (7)$$

measured with addition of protein aliquots of volume  $dV_i$  injected into the cell containing the mineral suspension.

In cases where only a fraction of the protein molecules, which adsorb to HAP, display a heat of adsorption that is measurable with calorimetry, the quantity  $M_t'$  is replaced by  $\alpha M_t'$  where  $\alpha$  is the fraction of all sites in which adsorption is accompanied by enthalpy change. The values of  $K_{\text{ads}}$ ,  $\Delta H$ , and  $\alpha$  are then derived by minimizing a calculated curve based on Eqn (6) to experimental titration curve measured in the calorimeter. If we assume that the sites A where adsorption is accompanied by heat change and B sites where adsorption is thermoneutral populate independently and each with a simple Langmuirian mechanism, which implies no interactions between the protein molecules that adsorb, and that the A site population nearly reaches saturation before significant population of the B sites occurs, then the fractional coverage of A is still well approximated by Eqn (5) with  $\alpha M_t'$  in place of  $M_t'$ .

### Equilibrium adsorption isotherm

In the adsorption experiments, known amounts of statherin in phosphate buffer were equilibrated for 4 h with HAP suspension at temperatures of 24 and of 37°C. After incubation, the protein concentrations in the supernatant following centrifugation of the suspension were determined using a Micro BCA protein assay reagent kit (Pierce), recording the absorbance at 562 nm on a safire<sup>2</sup> TECAN plate reader as described before.<sup>6</sup> The difference between the initial concentration and the measured one, i.e. the amount of adsorbed statherin, is normalized to the number of moles adsorbed per unit area by dividing it by surface area times the density of HAP in the suspension and plotted either *versus*  $[C]$  or  $\log[C]$ . The AI curve can be fitted to various models of adsorption to extract adsorption parameters such as the maximal coverage and adsorption equilibrium constant.

### NMR TECHNIQUES FOR THE STUDY OF PROTEIN STRUCTURE ON CRYSTALLINE MINERAL SURFACES

Solid-state NMR has been extensively used to investigate the structures of silica and alumina surfaces<sup>15–17</sup> and small molecules adsorbed to surfaces of catalysts.<sup>18–20</sup> In addition, <sup>13</sup>C MAS NMR spectroscopy has been used to study the incorporation of carbonate ions in bone and synthetic apatites,<sup>21</sup> and <sup>31</sup>P NMR experiments have been used to characterize phosphate species in inorganic precipitates in biological systems.<sup>22–24</sup>

Quantitative structural data can be obtained via orientational constraints and/or distance and torsion angle constraints. Angular constraints, usually obtained from magnetic interaction tensors located in the backbone of proteins

oriented in mono-domain lipid bilayers, have been used to determine the orientation of helices in transmembrane proteins embedded in lipid bilayers.<sup>25</sup> Distance and torsion angle constraints have been acquired for proteins in microcrystalline form<sup>26</sup> as well as in fibrils formed by  $\beta$ -amyloid peptides.<sup>27</sup>

The solid-state NMR techniques used to obtain structural data of proteins adsorbed onto biomaterial surfaces to date were reviewed before;<sup>28,29</sup> therefore, only a brief description of each technique is provided here. Dipolar recoupling with a windowless sequence (DRAWS)<sup>30</sup> experiments were used to determine the torsion angles around the protein backbone and its secondary structure. Preparation of double-quantum coherence using DRAWS dipolar recoupling (DQDRAWS) allows monitoring of the buildup of double quantum coherence as a function of the DRAWS mixing time to determine dipolar couplings and hence internuclear distances without interference from background single-quantum signals. As in the simple DRAWS experiment, the DQDRAWS filtering experiment can quantify the carbonyl–carbonyl distance and hence the backbone torsion angle  $\varphi$ .

Rotational echo double resonance (REDOR)<sup>31</sup> experiments were used to measure distances between the nuclear spins of different atoms on the protein and to elucidate secondary and tertiary constraints on the structure of the adsorbed protein. REDOR was also employed to measure distances between atoms on the protein side chains and on the surface of the crystal. In a recent work, we showed that the application of the REDOR experiment to certain  $I_2S$  spin systems (where  $I$  and  $S$  are heteronuclear spins) can be used for complete characterization of the internuclear distances in the spin triad. The reference measurement acquired typically in every REDOR experiment is utilized to obtain the homonuclear dipolar information in the  $I_2$  spin pair and the normalized dephasing measurement to deduce the two  $IS$  couplings and distances. The details of this REDOR–SEDRA approach were reviewed before.<sup>29</sup> Here, we mention briefly the principles of the technique and demonstrate its application in elucidating constraints on the structure of adsorbed statherin using as little as two separate measurements.

Simple excitation for dephasing of rotational-echo amplitudes (SEDRA)<sup>32,33</sup> was proposed for the measurement of the internuclear distance between two homonuclear spins by recovery of the dipolar interaction under magic angle spinning using a train of  $180^\circ$  pulses applied in synchrony with the rotation period. Performing REDOR measurements using alternating  $180^\circ$  pulses on  $I_2S$  spin triads with observation of the  $I$  spins renders the reference experiment an effective action describable by the SEDRA Hamiltonian. The SEDRA pulse experiment is sensitive to the relative orientation of the chemical shift anisotropies (CSAs) of the two homonuclear spins. In proteins, one can utilize this in order to extract the backbone dihedral angles between consecutive amino acid residues. In particular, the principle components of the carbonyl carbon CSA tensor have known directions in the peptide bond molecular frame. Therefore, the orientation of two CSA tensors can serve as a sensitive probe of the Ramachandran angles ( $\varphi, \psi$ ) between the two atoms. The distance between the carbonyl carbon atoms and the  $\varphi$  angle are

interdependent; so, the SEDRA dephasing basically depends solely on the two torsion angles.

## STATHERIN FUNCTION AT THE INTERFACE OF SALIVA AND TOOTH ENAMEL SURFACES

In this review, we summarize various studies that we carried out on a salivary protein, statherin, involved in several functions in the oral cavity but mostly associated with the regulation of HAP crystal nucleation and growth in saliva. Tooth enamel structural integrity is maintained through the supersaturation of saliva with respect to calcium and phosphate salts and through the lubricative action of proteins in the pellicle coating the oral surfaces.<sup>34–38</sup> The viscoelastic properties of statherin, PRPs, and mucins in the salivary pellicle reduce the mastication load on the tooth surfaces 20-fold.<sup>38,39</sup> Statherin and PRPs inhibit formation of mineral precipitates termed *accretions* on the tooth surface by inhibiting both spontaneous calcium phosphate precipitation and HAP secondary crystal growth.<sup>5,40–46</sup> Statherin can achieve these properties by binding calcium ions in solution and by adsorbing to HAP surfaces with a significant binding affinity and coverage.<sup>6,47,48</sup> The  $N$ -terminus of statherin contains a pSpSEE (where pS is phosphorylated serine) acidic motif that is also found in larger calcium-binding proteins such as osteopontin, as well as in biomineralization proteins that regulate calcium carbonate crystallization in lower organisms.<sup>49</sup> The effects of statherin on HAP crystal growth kinetics have been described before.<sup>5,50</sup> Nancollas has demonstrated that derivative peptides from the  $N$ -terminus of statherin display comparable functional activities in controlling HAP growth to the full length protein.<sup>4,51</sup> This work has stimulated investigations of the proximity and dynamics of side chains in an  $N$ -terminal fragment of statherin to the surface of HAP.<sup>52–54</sup>

The recognition and binding of statherin and PRPs by microbial organisms was later on linked with the onset of periodontal diseases, which are marked by the adherence and colonization of various bacteria to supra- and subgingival surfaces.<sup>55–57</sup> Statherin and the PRPs mediate the adhesion of bacterial species to the tooth surface.<sup>58–63</sup> These organisms preferentially adhere to immobilized statherin on HAP surfaces rather than to the free protein in solution,<sup>60,63</sup> leading to the hypothesis that surface adsorption exposes receptor sites in statherin to bacterial fimbriin binding. Recent studies identified the  $C$ -terminal residues 29–43 and residues 33–39 in statherin as binding domains for *Porphyromonas gingivalis* and *Fusobacterium nucleatum* fimbriae respectively.<sup>61,63</sup>

## DIFFERENTIAL MECHANISMS OF STATHERIN ADSORPTION TO HAP

The adsorption of statherin as well as other salivary proteins onto HAP were previously studied by equilibrium-binding isotherm measurements.<sup>4,5,47,48,64</sup> The work reviewed here highlights our recent studies<sup>6</sup> on the enthalpic and entropic contributions to the free energy of the adsorption and the heat capacity change involved in the adsorption process derived from measurements performed at different temperatures. ITC and equilibrium AI analysis were used to determine

thermodynamic parameters of statherin adsorption onto HAP crystals. The results are evident of two types of binding mechanisms having distinguishable enthalpy and entropy that we have used to generate a two-site model on the surface of HAP, providing a new insight into the mechanism of the statherin function on biological surfaces.

### Isothermal titration calorimetry (ITC)

The ITC experiment was carried out by repetitive injections of fixed volume of the protein (0.16 mM) into the calorimeter cell containing a sample of HAP crystals (2 mg/ml). Figure 1(a) shows the ITC measurement of adsorption at 25 °C, where the top graph depicts the heat signal change in the cell with time for statherin adsorption and the bottom graph shows the titration curve generated by time integration of the heat signal through the injections and plotted as a function of the ratio between total injected statherin concentration,  $C_t$ , and the maximal concentration of statherin sites on HAP,  $M_t'$ . The thermodynamic parameters of binding were derived from fitting the ITC curve after calculation of  $M_t'$  using information from separate measurements as outlined in the Section on

'Biophysical Methods for the Study of Protein Adsorption Thermodynamics onto Crystalline Mineral Surfaces'. The inflection point in the titration appears at a ratio of 0.23 between  $C_t$  and  $M_t'$ , although unity is expected, provided the AI measurement probes the same adsorption process as the ITC measurement. Moreover, at the end of the titration, one would expect the excess of protein that is added to the cell to be detectable as free protein. Yet, extension of the titration with 12 additional injections resulted in no change to the measured heat, and when the ITC cell content was taken out and the concentration of free protein determined, less than 10% of the total protein added was left in solution. On the basis of these observations and using additional experiments designed to confirm that there are no time scale differences in the mixing of protein with mineral in the two experiments and that the adsorption is a reversible process, we could distinguish two processes involved in the adsorption of statherin to HAP. An initial exothermic binding with an apparent heat of adsorption of about 3 kcal/mol followed by a thermoneutral one where the enthalpy of adsorption drops to around zero after injecting

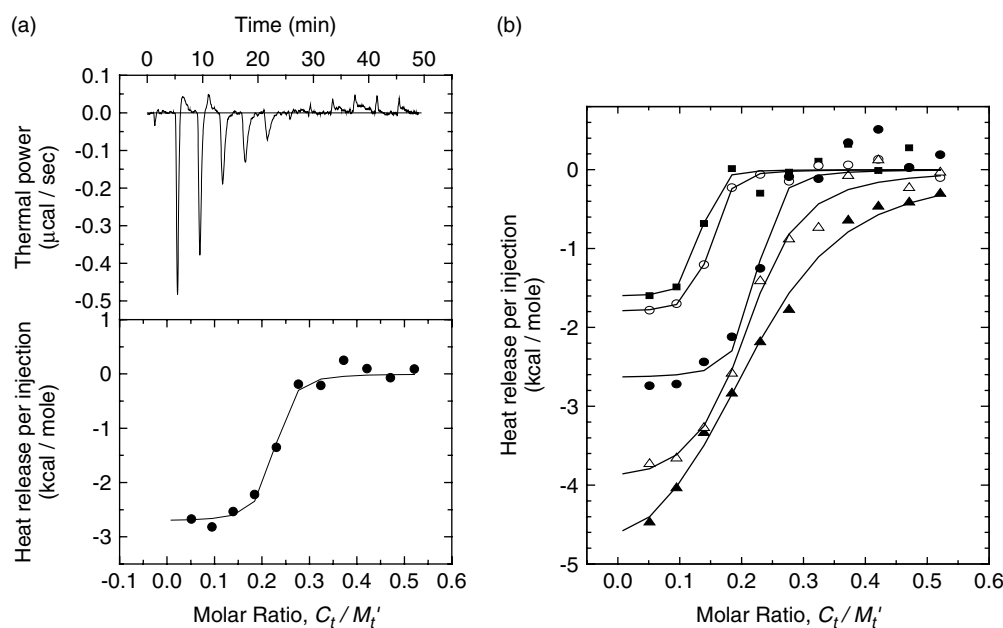


**Figure 1.** (a) ITC profile of the titration of HAP (2 mg/ml) with statherin (0.16 mM) performed at 25 °C in PB.<sup>6</sup> (b) Titration curves corrected for heat of dilution obtained for the titration of HAP (2 mg/ml) with statherin (0.16 mM) and depicted as a function of the molar ratio between the total injected statherin concentration,  $C_t$ , and the molar concentration of HAP adsorption sites,  $M_t'$ , performed at 15 °C (▲), 20 °C (△), 25 °C (●), 30 °C (○), and 37 °C (■) in PB. Data points were fit as described in the materials and methods.

**Table 1.** The apparent thermodynamic parameters for statherin adsorption onto HAP, obtained from ITC measurements at different temperatures

Temp (°C)	$\alpha$	$\Delta H$ (kcal/mole)	$T\Delta S^0$ (kcal/mole)	$\Delta G^0$ (kcal/mole)	$K$ (1/M)
15	0.21	$-5.4 \pm 0.4$	$2.1 \pm 0.3$	$-7.4 \pm 0.1$	$(4.3 \pm 0.8) \times 10^5$
20	0.18	$-4.0 \pm 0.4$	$4.1 \pm 0.2$	$-8.1 \pm 0.2$	$(1.1 \pm 0.4) \times 10^6$
25	0.21	$-2.7 \pm 0.1$	$6.8 \pm 0.2$	$-9.5 \pm 0.4$	$(9.5 \pm 5.8) \times 10^6$
30	0.13	$-1.8 \pm 0.2$	$8.0 \pm 0.2$	$-9.8 \pm 0.3$	$(1.2 \pm 0.6) \times 10^7$
37	0.11	$-1.6 \pm 0.4$	$8.5 \pm 0.3$	$-10.1 \pm 0.5$	$(1.4 \pm 1.0) \times 10^7$

only enough statherin to occupy about 30% of the sites on the HAP.

Titration curves for statherin adsorption onto HAP measured at a range of temperatures between 15 and 37 °C are shown in Fig. 1(b). The equilibrium association constant,  $K$ , the apparent adsorption enthalpy change,  $\Delta H_{\text{app}}$ , and the fraction of adsorption sites that have this enthalpy of adsorption,  $\alpha$ , were derived from minimization of a theoretical curve (Eqn (6)) against the calorimetry data.<sup>6</sup> The apparent standard Gibbs free energy change ( $\Delta G_{\text{app}}^0$ ) and the standard entropy change ( $\Delta S_{\text{app}}^0$ ) derived from these experiments are summarized in Table 1. The apparent enthalpy of adsorption increases from  $-5.4$  to  $-1.6$  kcal/mol (decreasing in absolute value), while the entropy of adsorption increases nearly fourfold between 15 and 37 °C. The Gibbs free energy change and the fraction of sites that are occupied through an exothermic adsorption vary to a lesser extent as the temperature is increased.

### Equilibrium adsorption isotherm measurements

The equilibrium AI for statherin onto HAP at 24 °C is shown in Fig. 2 as the moles of adsorbed protein per unit of surface area,  $N$ , versus log of the free statherin equilibrium concentration  $[C]$ . The points in the AI measurement are collected in different experiments with variable  $[C]$ , allowing the adsorption complex to equilibrate for 4 h.

A simple model based on independence of the adsorbing molecules gives rise to the Langmuir equation

$$N = \frac{KN_{\text{max}}[C]}{1 + K[C]} \quad (8)$$

It is identical to Eqns (1) and (4), describing the ITC experiment with the fractional coverage described as

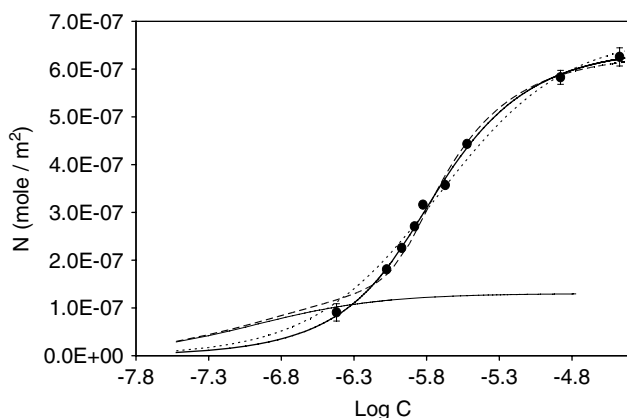


**Figure 2.** Adsorption isotherm data for the binding of statherin onto HAP (2 mg/ml at 1.42 ml) at 24 °C plotted versus the log of the equilibrium concentration.<sup>6</sup> The dotted line is the best fit to the Langmuir model. The solid bold line is the best fit to the bimodal model, where 21% of the protein molecules bind according to a Langmuir model and 79% according to an attractive model, as given in Eqns (10–12). The dashed line is that same fit to bimodal model but with applying  $\alpha$  and  $K_A$  values obtained from the ITC measurements (Table 2, ITC bimodal fit). The solid thin line represents generated adsorption isotherm to A sites, applying  $\alpha$  and  $K_A$  values from ITC at 25 °C (Table 1).

$\theta = N/N_{\text{max}}$ . The data in Fig. 2 are reasonably well fit by this simple first-order Langmuir AI, as shown by the dotted line, with best-fit values of  $K = 5.0 (\pm 1.0) \times 10^5 \text{ M}^{-1}$  and  $N_{\text{max}} = 6.7 (\pm 0.3) \times 10^{-7} \text{ mol m}^{-2}$ . These values are within the same order of magnitude as those previously reported,<sup>5</sup> with minor differences that may be attributed to variations in solution conditions. The asymptotic value of  $N_{\text{max}}$  indicates saturation of the surface of HAP by the first layer of protein molecules. Addition of more molecules did not result in change to the isotherm curve and therefore we consider the possibility of multilayer adsorption unlikely.

The  $M_t'$  value (calculated using this  $N_{\text{max}}$  value in Eqn (3)) is much larger than the concentration of sites that have a measurable heat of adsorption according to the ITC data, as reflected in the low values for  $\alpha$  (0.11–0.21) in Table 1. That is, the calorimetric results do not coincide with the binding isotherm data in that the latter gives a much higher saturation coverage when both are independently analyzed assuming a first-order Langmuir AI. Also, the ITC data give an equilibrium constant that is more than tenfold larger than the isotherm data. A very similar equilibrium AI was also measured at 37 °C (data not shown).<sup>6</sup> The saturation coverage and equilibrium constant are almost independent of temperature.

The calorimetric results were combined with the equilibrium AI data to estimate the enthalpy associated with adsorption versus fractional coverage of surface sites,  $N/N_{\text{max}}$ , at 25 and 37 °C. The results are shown in Fig. 3. The  $y$ -axis conversion from moles injected to moles adsorbed was made using the equilibrium AI (Fig. 2), with the assumption that equilibrium was reached after each calorimetry injection. From the figure, it is clearly seen that at low coverage the adsorption is driven by an exothermic enthalpy, but that the heat of adsorption drops to near zero by ~40% of saturation at 25 °C and only ~20% of saturation at 37 °C.

We interpret these results and those in Table 1 as indicating that there are two types of sites on the HAP: A-type sites with a measurable heat of adsorption and a larger equilibrium constant which populate first but which only

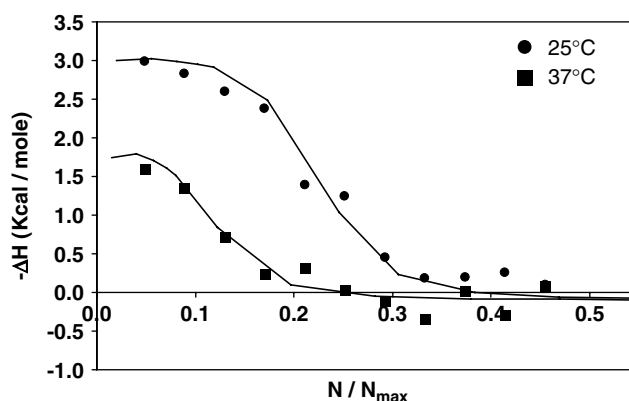


**Figure 3.** Plot of heat of adsorption ( $-\Delta H$  per mole of adsorbed protein) versus coverage at 25 °C (●) and 37 °C (■). The data was fit using Eqns (12–13) and applying the  $\alpha$  and  $K_A$  values from the ITC for A sites (Table 1) and the rest of the parameters from the bimodal fit to the isotherm data<sup>6</sup> (Table 2, ITC bimodal fit).

account for  $\sim 16(\pm 5)$  % of the total sites; and B-type sites with no measurable heat of adsorption and a far weaker binding constant. Such a two-state model is not surprising, since it is well known that protein adsorption onto surfaces is not a simple one-step process.<sup>14,65–67</sup> Note that the B sites either have a heat of adsorption that is really negligible or, since the calorimeter is insensitive to heat that is deposited too slowly, they may also have a substantial heat of adsorption but simply populate too slowly to give measurable heat.

From Table 1, it is clear that entropy makes the dominant contribution to the free energy of adsorption even at low coverage where adsorption is exothermic. Adsorption beyond  $\sim 30\%$  of saturation appears to be entirely due to the increase in entropy, unless any heat of adsorption is delivered too slowly to measure. We also fit the binding isotherm data of Fig. 2 with a simple model involving two first-order Langmuir-type adsorption sites, each populated independently and with different equilibrium constants. In this case, the overall coverage is expressed as the sum of the two processes and Eqn 4 becomes

$$\theta_{\text{total}} = \alpha \cdot \theta_A + (1 - \alpha) \cdot \theta_B = \alpha \frac{K_A[C]}{1 + K_A[C]} + (1 - \alpha) \frac{K_B[C]}{1 + K_B[C]} \quad (9)$$

where  $\alpha$  is the fraction of sites that are A type.

Fitting the binding isotherm data in Fig. 2 to this model gave similar values for  $K_A$  and  $K_B$  with no noticeably better quality fit than a single-site model. However, the data could be fit better by such a model if we assumed that the equilibrium constant for the B sites,  $K_B$ , increases with increasing coverage of B sites. In this case,  $K_B$  must be treated as a function of  $\theta$  and therefore becomes  $K'_B$ :

$$K'_B = K_B + \beta\theta = \frac{\theta_B}{(1 - \theta_B)[C]} + \beta\theta_B \quad (10)$$

where  $\beta$  is a correction term to the equilibrium constant that accounts for attractive interactions between the assembled molecules and is proportional to  $\theta$ . To express the coverage dependence on  $[C]$  in the process of adsorption to site B, Eqn (9) can be rearranged as follows:

$$\theta_B = \frac{1}{2\beta[C]} \left[ \beta[C] - K'_B[C] - 1 \pm \sqrt{(1 + K'_B[C] - \beta[C])^2 + 4K'_B\beta[C]^2} \right] \quad (11)$$

**Table 2.** Equilibrium isotherm parameters for statherin adsorption onto HAP calculated from best fits of the Langmuir (Eqns 1, 8) and bimodal (Eqns 9, 11) equilibrium binding isotherms models to the measured equilibrium binding isotherms at 24 and 37 °C. ITC = bimodal fit applying  $\alpha$  and  $K_A$  values obtained from ITC data (Table 1) at the closest temperature

Temp (°C)	Langmuir		Bimodal				
	$N_{\text{max}}$ ( $10^{-7}$ mol/m <sup>2</sup> )	$K$ ( $10^5$ /M)	$N_{\text{max}}$ ( $10^{-7}$ mol/m <sup>2</sup> )	$\alpha$	$K_A$ ( $10^5$ /M)	$\beta$ ( $10^5$ /M)	$K_B$ ( $10^5$ /M)
24	$6.7 \pm 0.3$	$8.0 \pm 1.0$	$6.4 \pm 0.2$	0.21	$7.6 \pm 1.0$	$6.6 \pm 3.0$	$2.4 \pm 0.5$
24 (ITC)	–	–	$6.3 \pm 0.2$	0.21 (ITC)	$95 \pm 58$ (ITC)	$8.5 \pm 4.0$	$0.5 \pm 0.2$
37	$6.3 \pm 0.3$	$7.4 \pm 0.9$	$6.0 \pm 0.2$	0.11	$9.0 \pm 2.0$	$13 \pm 3.0$	$2.6 \pm 0.5$
37 (ITC)	–	–	$6.0 \pm 0.2$	0.11 (ITC)	$140 \pm 100$ (ITC)	$13 \pm 3.0$	$1.4 \pm 0.5$

We then simply substitute the expression for  $\theta_B$  in Eqn (8) with the one in Eqn (10). Figure 2 shows that such a model fits the isotherm very well (solid bold line).

The  $K_A$  value determined by AI is tenfold smaller than the equilibrium constants determined from ITC fitting at similar temperatures (Table 1). This is probably because of the very low population of the A-type sites that have a measurable heat of adsorption ( $\sim 16\%$  of the total), coupled with the fact that the adsorption isotherms have no data points below this coverage. This renders their fits very insensitive to the parameters that define the A-type sites. For example, if the much more populous B sites have some heterogeneity, it is likely that the two different types of sites that result from fitting the isotherm data correspond to subpopulations of B sites, missing the contribution from A sites almost entirely.

For the purpose of comparison between the equilibrium-binding isotherm and the ITC experiment, we have generated a putative binding isotherm of process A by applying  $K_A$  and  $\alpha$  values that were obtained from the ITC measurement. Figure 2 depicts the measured binding isotherm (solid data points) and the simulation for process A alone (solid thin line) using the parameters determined for it by fitting the ITC data at the closest temperature (25 °C), listed in Table 1. It is notable that process A reaches saturation rapidly and its contribution to the binding isotherm is at the early stages of the adsorption where the equilibrium concentrations are low. Owing to lack of sensitivity of the BCA assay at those low protein concentrations, we could not conduct a binding isotherm mimicking the ITC experiment.

Figure 2 also displays a fit of the binding isotherm data using another bimodal model in which both the  $K_A$  and  $\alpha$  values were assumed to be those determined from the best-fit to the ITC measurements in Table 1 (dashed line). The other three parameters were determined to give the best fit to the data, and are listed in Table 2. We call this the 'ITC bimodal model'. Given the data statistics, there is no significant difference in the quality of this fit and that of the bimodal fit given above that had more adjustable parameters. Both give good fits to the data. They differ strongly only below 15% of saturation, where there are no data. This new fit represents the best bimodal model that is most consistent with all of the data (i.e., both the ITC data and AI). The binding isotherm at 37 °C was similarly analyzed and the recovered parameters are given in Table 2.

To isolate the coverage change in process A relative to the total coverage in Eqn (10), one can write the differential

change in process A versus the total coverage:

$$d \left( \frac{N_A/N_{\max}}{N/N_{\max}} \right) = \alpha \cdot \left( \frac{d\theta_A}{d\theta_{\text{total}}} \right) \quad (12)$$

This is advantageous when we would like to follow exclusive contributions due to process A that involves an enthalpy change, while process B involves no change in heat. This function is utilized to extract the actual binding enthalpy change due to the association,  $\Delta H_{\text{assoc}}$ , of process A from measurement of apparent enthalpy change  $\Delta H_{\text{app}}$  with coverage as follows:

$$\Delta H_{\text{app}}(N/N_{\max}) = \Delta H_{\text{assoc}} \cdot \frac{d(N_A/N_{\max})}{d(N/N_{\max})} \quad (13)$$

The experimental data in Fig. 3 was fit with the above equation, applying the  $K_A$  value from the ITC for A sites (Table 1) and the rest of the parameters from the ITC bimodal model to the isotherm data. The resulting value of  $\Delta H_{\text{assoc}}$  from this fitting is  $-3.3$  and  $-2.1$  kcal/mol for 25 and 37 °C respectively. These values are slightly higher than the ITC  $\Delta H_{\text{app}}$  values (Table 1). This is because a few B-type sites are also being populated during the ITC injections, so that the A-type sites only correspond to about 80% of the total adsorption during ITC in this model (Fig. 2). To give the same amount of heat, the adsorption heat per mole of A-type adsorbate must then be scaled up by 25%.

### The effect of temperature on the adsorption enthalpy

The change in the reaction enthalpy with temperature defines the reaction's heat capacity change,  $\Delta C_p$ . Its value for statherin adsorption on A sites of HAP was calculated by plotting the adsorption enthalpies measured by ITC at different temperatures (data not shown).<sup>6</sup> The positive  $\Delta C_p$  observed for statherin adsorption to HAP are discussed in Section 'Views of Statherin Structure and Assembly Mechanisms on HAP Surfaces'.

### STRUCTURAL NMR MEASUREMENTS OF FREE AND HAP-BOUND STATHERIN

Simulations of the N-terminus secondary structure based on its amino acid sequence predicted the existence of

an  $\alpha$ -helix in this region. Circular dichroism and NMR measurements<sup>68,69</sup> found that in water statherin is structurally disordered while under less polar conditions, in 50% trifluoroethanol (TFE)/water mixture, statherin assumes an  $\alpha$ -helical structure at the N-terminal region (residues 1–16), a polyproline type II ( $P_{II}$ ) helix in the intermediate region (residues 19–35), and a  $3_{10}$  helix in the C-terminal region (residues 36–43).<sup>68</sup> We have carried out 2D nuclear Overhauser enhancement spectroscopy (NOESY) and Total Correlation Spectroscopy (TOCSY) experiments of statherin in phosphate buffer solution and in phosphate buffer solution with 4 mM of calcium chloride added at temperatures of 285 and 278 K. All 2D spectra of statherin (data not shown) exhibit limited cross peaks at the amide–amide region, demonstrating no substantial structuring of dissolved statherin in phosphate buffer with and without the addition of calcium ions.

Statherin samples are prepared for solid-state NMR measurements by adsorbing quantities of protein that are lower than the saturation coverage to minimize interference from intermolecular interactions in the structural measurements. The accumulated measurements are successful in providing us with a solid basis for construction of the three-dimensional model of statherin's structure at its adsorbed state. Initial investigation of full length surface-bound statherin provided us with secondary structure information of the protein's N-terminus.<sup>70</sup> Recent work achieved both secondary structure data in the C-terminal bacterial binding domain and tertiary structural constraints on the surface-bound protein.<sup>71</sup>

### Backbone structure of the N-terminal HAP-binding domain

To probe the molecular backbone structure of statherin on HAP under buffered, hydrated conditions, isotopic labels were selectively incorporated at the pS2, pS3, F7, L8, I11, and G12 backbone carbonyl carbons or nitrogens in five different samples of statherin. Details of all DQDRAWS and REDOR measurements on the N-terminus of statherin were reported elsewhere.<sup>70</sup> Here, we show, for example, the backbone  $\phi$  angle determination with the DQDRAWS techniques at the pS2pS3 positions. In Fig. 4(a), the buildup of DQ coherence

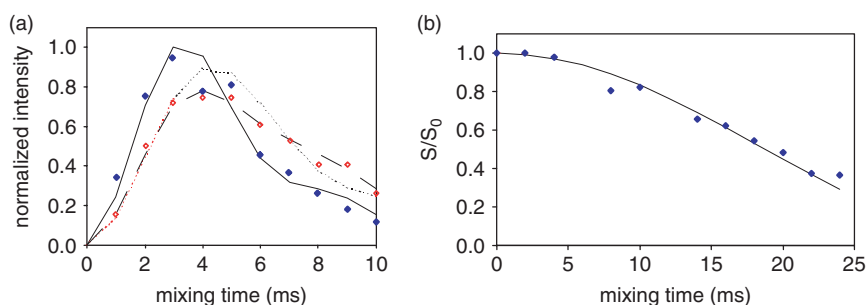


**Figure 4.** (a) DQDRAWS buildup curves for hydrated, surface-adsorbed pS<sub>2</sub>pS<sub>3</sub> statherin (◆), lyophilized, bound pS<sub>2</sub>pS<sub>3</sub> statherin (◇), and simulations for  $\phi$  torsion angles of  $-60^\circ$  (—),  $-85^\circ$  (⋯), and a combination of 35%  $\alpha$ -helix ( $-57^\circ$ ) and 65%  $\beta$ -sheet ( $-120^\circ$ ) (---). The increase in torsion angle on lyophilization correlates well with the loss of  $\alpha$ -helical secondary structure. (b) REDOR dephasing curves for hydrated, surface-adsorbed pS<sub>3</sub>F<sub>7</sub> statherin (◆) and simulations for a carbon–nitrogen distance of 4.2 Å (—). The pS<sub>3</sub>F<sub>7</sub> distance across the hydrogen bond fits best to a distance of 4.2 Å, indicating that the region is well described by an ideal  $\alpha$ -helix.<sup>70</sup>

is plotted for statherin adsorbed onto HAP crystals and fully hydrated (solid blue diamonds) and for lyophilized samples (empty red diamonds). The solid line drawn through the hydrated protein data is the DQDRAWS simulation for an  $\alpha$ -helical secondary structure.  $^{13}\text{C}$ - $^{15}\text{N}$  REDOR was used to measure the (*i*) to (*i* + 4) distances in pS3F7 and L8G12 labeled protein samples. As an example measurement, we show the carbonyl-amide REDOR measurement in the pS3F7 labeled protein (Fig. 4(b)). The composite results defined this *N*-terminal, 12 amino acid-long HAP-binding domain as  $\alpha$ -helical on HAP surface. The strongly acidic N-6 region displays a nearly ideal  $\alpha$ -helical distance of 4.2 Å across the pS3F7 hydrogen bond, while the helix across the L8G12 hydrogen-bonding position has a longer pitch at 4.8 Å.<sup>70</sup>

The  $\alpha$ -helix has been previously suggested as a general structural mechanism for aligning acidic side chain residues with HAP, either through lattice matching or through more general electrostatic complementarity.<sup>9</sup> Our data are consistent with this hypothesis and further point to the possible importance of bridging water in protein-HAP recognition.

The dynamic properties of the immobilized protein are a critical aspect of molecular recognition at the protein biomaterial interface, and related to the function of proteins once adsorbed. Measurements of the dynamic properties of statherin in the presence and absence of water provide valuable evidence that a binding footprint is centered on the acidic residues in the *N*-terminal pentapeptide region. The  $^{13}\text{C}$  rotating frame relaxation,  $T_{1\rho}$ , values remain largely unchanged for the phosphoserines, indicating little or no motion is present in either the lyophilized or hydrated states. However, the  $T_{1\rho}$  relaxation constants are considerably shorter in the hydrated samples at the F7, L8, I11, and G12 positions, indicating motion on the kilohertz time scale when water is present. Figure 4(a) shows changes to the DQ buildup curve in the pS2-pS3 doubly carbon-labeled statherin sample under hydrated conditions *versus* lyophilized conditions and normalized to the natural abundance methyl region to account for any differences in the amounts of bound protein.

### Secondary structure of the C-terminal bacterial binding domain

Placement of isotopic labels for REDOR and DQDRAWS NMR studies of the 15 *N*-terminal amino acids was guided by solution NMR studies and circular dichroism data, which indicated that the HAP-recognition region was very likely structured as an  $\alpha$  helix. In the case of the *C*-terminal domain, little prior knowledge of local secondary structure existed to guide placement of isotopic labels. We therefore implemented structural modeling as a guideline for placement of isotopic labels at locations with high probabilities for significant measurements of secondary structural elements and tertiary folding constraints.

Since no structural homologues were available for the sequence of human statherin, the *ab initio* protocol of the structure modeling program ROSETTA<sup>72</sup> was used to generate structural models of the protein. Nearly all 1000 models in the starting set predicted that the protein's *N*-terminus (residues 3-15) is  $\alpha$ -helical, as previously demonstrated

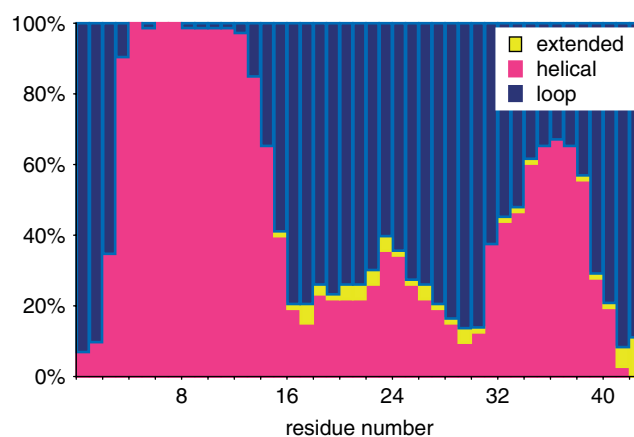


**Figure 5.** Modeling statherin structure using the ROSETTA *ab initio* algorithm.<sup>71</sup> The following histogram shows the percentage of the three basic secondary motifs along the backbone in the predicted 31-model cluster. This representation of the prediction data with other information that emphasizes the common features between the models were used to select sites on the protein for incorporation of isotope-enriched nuclei and solid-state NMR experimental investigations.

experimentally. The models were then divided into subsets based on their structural similarity with the largest cluster consisting of 31 models. The histogram showing the percentage of an extended, helix, or loop backbone secondary structure for this subset is depicted in Fig. 5. In this representation of the secondary motif distribution, an  $\alpha$ -helical segment at the *C*-terminus of the protein (residues 32-40) is predicted. The intermediate segment has a higher structural dispersion that can be identified at residues G19 and P31. Selection of an isotope labeling scheme for the protein sample was derived from analysis of the torsion angles and distances between pairs of atoms across the models and using only positions that are conserved in the protein between different species. Histograms of these structural parameters for the selected label positions are given in Fig. 6. Two consecutive carbonyl atoms on residues 33 and 34 were  $^{13}\text{C}$  labeled and an amide on tyrosine 38 was  $^{15}\text{N}$  labeled to extract the secondary structure in this region. Replacement of hydrogen with a fluorine atom on the 4' position of proline 23 was employed for long-range carbon-fluorine distance measurements between carbonyl carbon labels in the *C*-terminus and the sidechain of a proline near the protein center. The following labels, DpSpSEEKFLRRIGRFGYGY[2- $^{13}\text{C}$ ]G19PYQ[4'- $^{19}\text{F}$ ]P23VPEQPLYPQ[1- $^{13}\text{C}$ ]P33[1- $^{13}\text{C}$ ]Y34QPQ[1 $^{15}\text{N}$ ]Y38 QQYTF were therefore incorporated in the synthesis of statherin.

Using this labeling scheme,  $^{13}\text{C}$ - $^{15}\text{N}$  REDOR measurements provided us with the ( $\varphi, \psi$ ) angles, the carbon-carbon (CC) distance, and the carbon-nitrogen (CN) distances. Additional information relating the CN dipolar vector to the CSA principal axis system enabled the geometry of the  $^{13}\text{C}$ - $^{13}\text{C}$ - $^{15}\text{N}$  spin triad to be fully characterized. The reference experiment ( $S_0$ ) usually carried out as part of the REDOR measurement is analogous to a SEDRA experiment and therefore induced recoupling of the carbonyl carbon

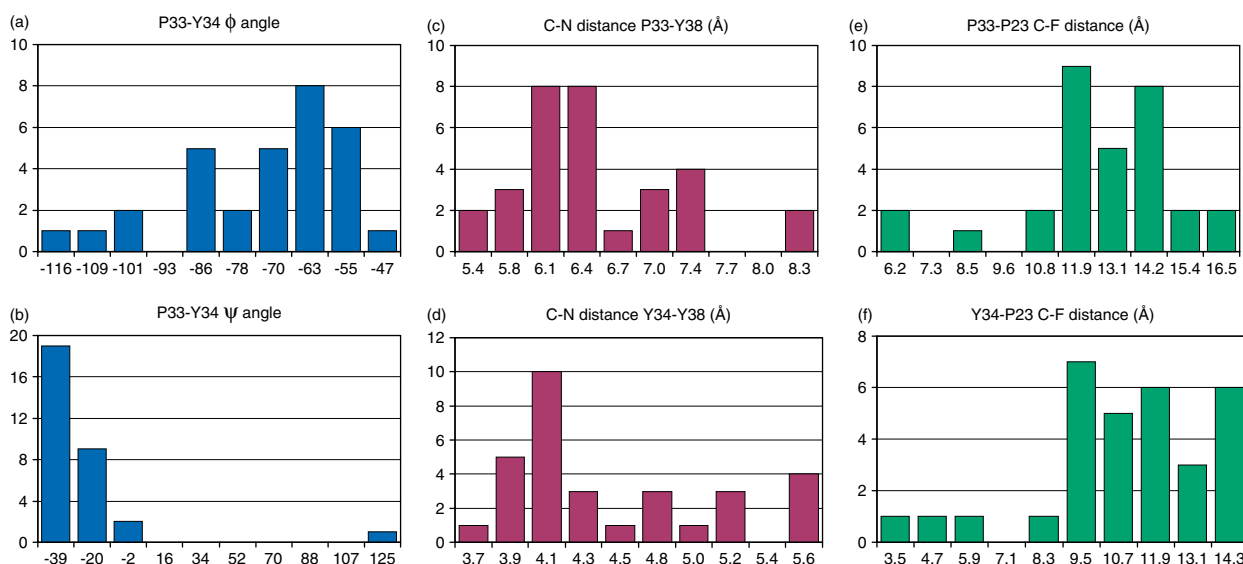


**Figure 6.** Histograms showing distribution of torsion angles and distances between labels across the 31-model cluster.<sup>71</sup> (a)  $\Phi$  angle and (b)  $\Psi$  angle values for the backbone torsion angles between the two carbonyl labels  $[1-^{13}\text{C}]\text{P33}$  and  $[1-^{13}\text{C}]\text{Y34}$ . Nitrogen–carbon distances between the (c)  $[^{15}\text{N}]\text{Y38}$  label and the  $[1-^{13}\text{C}]\text{P33}$  label and between the (d)  $[^{15}\text{N}]\text{Y38}$  label and the  $[1-^{13}\text{C}]\text{Y34}$  label. Fluorine–carbon distances between the (e)  $[4'-^{19}\text{F}]\text{P23}$  label and the  $[1-^{13}\text{C}]\text{P33}$  label and between the (f)  $[4'-^{19}\text{F}]\text{P23}$  label and the  $[1-^{13}\text{C}]\text{Y34}$  label.

dipolar couplings due to a nonzero *difference* CSA tensor (Fig. 7(a)). Analysis of the carbonyl carbon signal dephasing curve obtained in the  $S_0$  experiment in terms of the torsion angles between the two labels gave rise to a pair of angles without ambiguity. The resulting angles are consistent with a compact  $\alpha$ -helical conformation of the backbone at this position (Fig. 8(a)). The  $^{13}\text{C}$ – $^{15}\text{N}$  REDOR curve (Fig. 7(b)) gave rise to a  $[1-^{13}\text{C}]\text{Y34}$ – $[^{15}\text{N}]\text{Y38}$  distance of 4.0 Å (Fig. 8(b)) that is indicative of a hydrogen bond stabilizing the  $\alpha$ -helical structure deduced from the  $S_0$  experiment. Following extraction of the  $[1-^{13}\text{C}]\text{P33}$ – $[^{15}\text{N}]\text{Y38}$  distance (Fig. 8(c)), the angle between the  $[1-^{13}\text{C}]\text{Y34}$ – $[^{15}\text{N}]\text{Y38}$  and the  $[1-^{13}\text{C}]\text{P33}$ – $[^{13}\text{C}]\text{Y34}$  vectors was determined to be  $95(\pm 5)^\circ$ , implying that the hydrogen bond is nearly parallel to the helix axis. In case of a compact backbone conformation in particular, this typical  $\text{C}(i-1) - \text{C}(i) - \text{N}(i+4)$  labeling scheme can be informative and extends the information derived due to a triangulation effect. In special cases, where the carbonyl CSA orientation in the peptide molecular axis is not known, the measurement is complicated by added unknown parameters. It is noted that, whenever an extended conformation of the backbone exists, a  $^{13}\text{C}$ – $^{13}\text{C}$ – $^{15}\text{N}$  spin triad is not expected to be fully determined. Owing to the low sensitivity of REDOR NMR to  $^{13}\text{C}$ – $^{15}\text{N}$  distances larger than 7 Å, a negative result, i.e. no REDOR dephasing, would be expected, which would exclude the presence of a compact conformation in favor of an extended one.

### Tertiary constraints on statherin fold

The  $[4'-^{19}\text{F}]$  label inserted on residue P23 provided us with another triangulation using long range  $^{13}\text{C}$ – $^{19}\text{F}$  REDOR measurements of the  $^{13}\text{C}$ – $^{13}\text{C}$ – $^{19}\text{F}$  spin triad. The complete characterization of the spin interactions in the  $^{13}\text{C}$ – $^{13}\text{C}$  spin pair was utilized to extract from the REDOR dephasing experiment both, the two carbon–fluorine (CF) distances

and their vector orientation, relative to the carbonyl carbons CSA principal axis system. The  $^{13}\text{C}$ – $^{19}\text{F}$  REDOR curve (Fig. 7(c)) demonstrates that the C-terminus labels are in proximity to the fluorine label, constraining the distances of these labels from the  $[4'-^{19}\text{F}]\text{P23}$  label to 8.8 and 10.3 Å (Fig. 8(d) and (e)). The two labeled carbonyl carbons are unresolved in the  $^{13}\text{C}$  NMR spectra, and thus the assignment of the closer carbon atom cannot be made. The detectable carbon–fluorine distances demonstrate that the C-terminus  $\alpha$ -helical domain is folded back onto the center domain of the protein containing residue P23.

### Proximity of protein sidechains to crystal surfaces

The strength of interaction between statherin and the HAP surfaces relies on bonds created between side chains on the protein and exposed groups on the surfaces to which that protein adsorbs. Distance measurements between side chains on the SN15 derivative and NMR active  $^{31}\text{P}$  atoms on the HAP surface were used to learn about the proximity of particular residues to the surface. Nitrogen–phosphorous (NP) REDOR measurements were carried out on a  $^{15}\text{N}_\epsilon(\text{K6})$ -labeled SN15 sample.<sup>52,53</sup> Analysis of REDOR measurement in the case where an atom on the protein might be coupled to several phosphate groups on the surface was detailed in two publications.<sup>53,73</sup> Analysis of the REDOR data yields at least two possible geometries of the  $^{15}\text{N}$  spin to multiple  $^{31}\text{P}$  spins in the HAP surface. The relatively short distances to the phosphorous atom imply possible hydrogen bonds created upon adsorption. A  $\chi^2$  analysis of the data given before<sup>53</sup> is shown in Fig. 9(a). It assumes a nitrogen–phosphorous–phosphorous (NPP) system with a  $^{31}\text{P}$ – $^{31}\text{P}$  effective dipolar coupling of 600 Hz, and shows a well-defined minimum for  $^{15}\text{N}$ – $^{31}\text{P}$  distances of 3.8 and 4.8 Å from the  $^{31}\text{P}$  spins (Fig. 9(a), filled circles). In addition, to the simplified three spin model, we have simulated a  $^{15}\text{N}$  spin

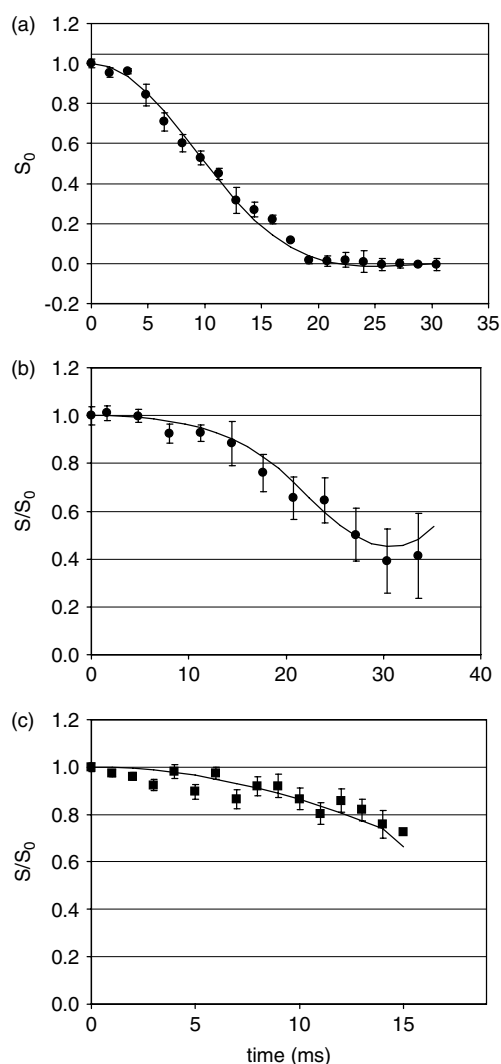


**Figure 7.**  $^{13}\text{C}$  NMR decay curves showing the carbon signal intensity as a function of the length of time for which the SEDRA and REDOR pulses are applied.<sup>71</sup> (a)  $^{13}\text{C}$  signal decay in the REDOR reference experiment ( $S_0$ ) showing SEDRA-type dephasing behavior due to recoupling of the  $^{13}\text{C}$ – $^{13}\text{C}$  dipolar interaction. The solid line is the best fit simulation of this decay curve, varying the backbone dihedral angles ( $\Phi, \Psi$ ) exclusively. (b)  $^{13}\text{C}$ – $^{15}\text{N}$  and (c)  $^{13}\text{C}$ – $^{19}\text{F}$  REDOR NMR decay curves showing the carbon signal intensity as a function of the length of REDOR mixing time normalized to the respective  $S_0$  experiment. Solid lines indicate the best fits to these decay curves based on  $\chi^2$  analysis of simulations, varying the three free parameters that these calculations depend on, as described in Fig. 8. Data for the  $^{13}\text{C}$ – $^{15}\text{N}$  and  $^{13}\text{C}$ – $^{19}\text{F}$  REDOR data were measured at different fields. Here only the  $S_0$  for the  $^{13}\text{C}$ – $^{19}\text{F}$  REDOR experiment is conveniently shown. The  $S_0$  data for the  $^{13}\text{C}$ – $^{15}\text{N}$  REDOR measurement was published elsewhere (See Fig. 7 in the support information of Ref. 71). It shows an extended decay time and was similarly fit to the backbone torsion angles in consistency with the data shown here.

from the lysine side chain approaching two spins on the (004) crystal plane of HAP, as shown in Fig. 9(b). These spins are connected to six other spins at distances shown in Table 3

in Ref. 48. We obtained a fit similar to the one obtained from the simple model, described above, but with slightly different  $^{15}\text{N}$ – $^{31}\text{P}$  distances of 3.9 and 4.4 Å (Fig. 9(a), filled pentagons).

Although acidic and basic amino acids are thought to constitute the primary means by which proteins interact with apatitic surfaces, the role of aromatic rings has attracted our attention. Constant composition techniques have shown that phenylalanine has the highest HAP affinity constant of the nonpolar amino acids,<sup>74</sup> and, because the *N*-terminus of statherin has two phenylalanines, the role these residues play in surface recognition is of interest.

Two samples containing  $^{13}\text{C}$  labels on the phenyl ring of phenylalanine 7 (F7) and phenylalanine 14 (F14) were bound to HAP.<sup>54</sup> Isotropic chemical shifts, CSAs, NMR line width information,  $^{13}\text{C}$  rotating frame relaxation measurements, as well as direct detection of correlations between  $^{13}\text{C}$  spins on protein side chains, and  $^{31}\text{P}$  spins in the crystal surface with  $^{13}\text{C}$ – $^{31}\text{P}$  REDOR NMR show that, in the peptide fragment derived from the *N*-terminal 15 amino acids of salivary statherin (i.e. SN15), the side chain of the phenylalanine nearest to the *C*-terminus of the peptide (F14) is dynamically constrained and oriented near the surface, whereas the side chain of the phenylalanine located in the middle of the peptide (F7) is more mobile and is oriented away from the HAP surface, as shown in Fig. 10. The relative dynamics and proximities of F7 and F14 to the surface together with prior data obtained for the side chain of SN15's unique lysine (K6) were used to construct a new picture for the structure of the surface-bound peptide and its orientation to the crystal surface.

## VIEWS OF STATHERIN STRUCTURE AND ASSEMBLY MECHANISMS ON HAP SURFACES

ITC and equilibrium AI results shown in this study indicate that only a fraction of the protein adsorbs to the mineral surface with detectable heat and that most of the protein adsorbs through a process that is accompanied by no detectable heat change. The following discussion interprets this finding in the context of a two-binding-site model that is implicitly based on the assumption of monolayer coverage limits. The protein molecules may adsorb onto the surface through a variety of orientations; however, from the solid-state NMR results, it is clear that the globular structure of the protein is intact even if it binds through different parts of its external surface. Molecular simulation programs are emerging that strive to predict protein structure and orientation on surfaces.<sup>75,76</sup> The binding isotherm shown here (Fig. 2) exhibits a single deflection point in the curve and not the typical detectable steps in concentration at monolayer completion that is characteristic of multilayer adsorption.<sup>14,77</sup>

The adsorption of statherin to HAP is an exothermic process. However, this heat is relatively low and it is in fact the entropy that makes the dominant contribution to the free energy of adsorption. Moreover, entropy is the only contribution to the adsorption process to site B. For all temperatures above 20 °C, the entropy contribution dominates adsorption even at the lowest fractional coverage

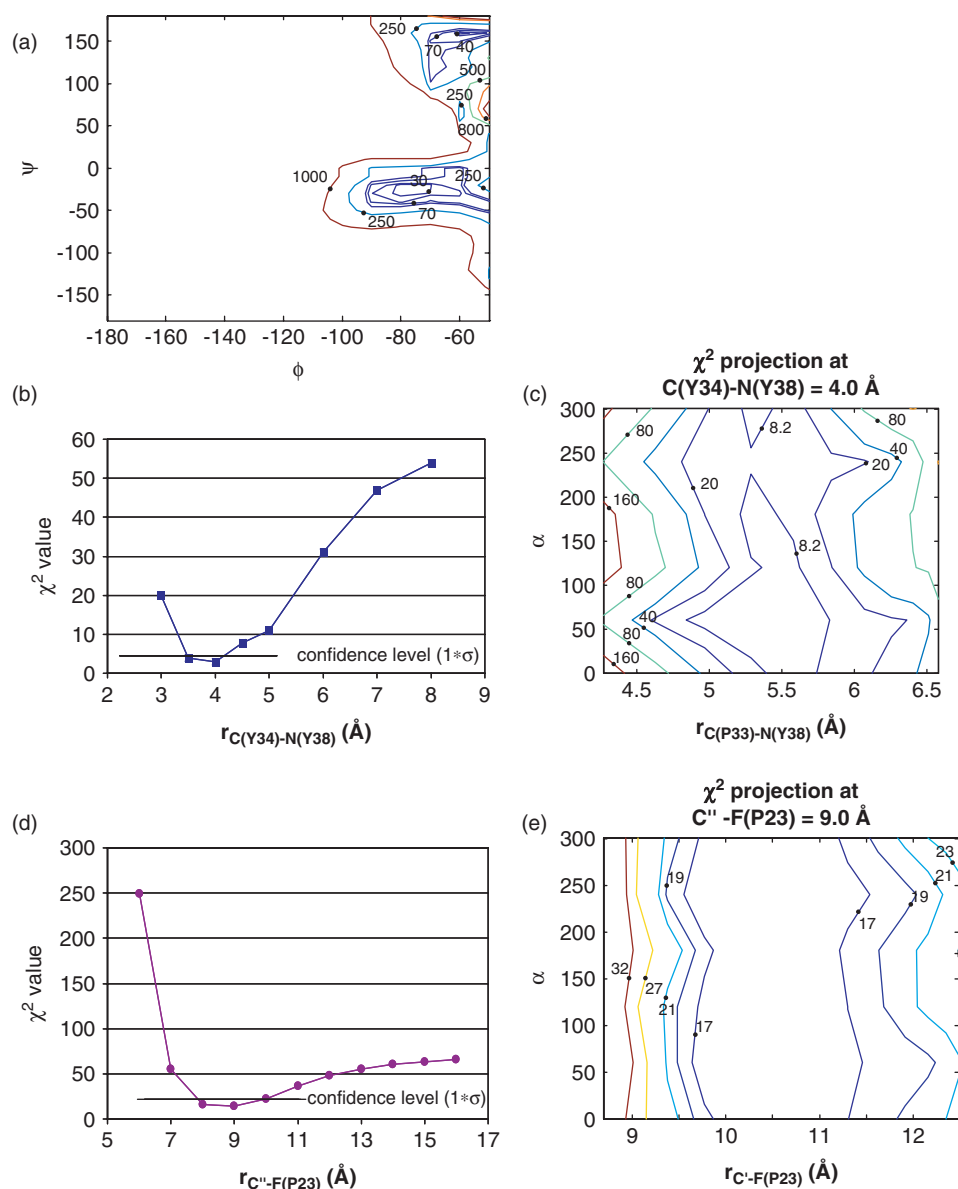


**Figure 8.**  $\chi^2$  analysis of simulated SEDRA and REDOR NMR curves to the experimental data shown in Fig. 7. The simulations of the SEDRA data (the REDOR  $S_0$  experiment) were carried out with the Ramachandran angles ( $\Phi, \Psi$ ) as free parameters ( $\chi^2 = \chi^2(\Phi, \Psi)$ ). The simulations of the REDOR data were carried out with the length of the heteronuclear dipolar vectors and the angle  $\alpha$  as free parameters ( $\chi^2 = \chi^2(r_{C(P33)-F \text{ or } N}, r_{C(Y34)-F \text{ or } N}, \alpha)$ ). The angle  $\alpha$  is the rotation angle of the heteronuclear vectors around the CC vector and defines the polar angles of these vectors in the C(P33) carbonyl carbon CSA frame. The resultant dephasing curves were normalized to the calculated  $S_0$  curve to obtain standard S/ $S_0$  curves. (a) Contour map of the  $\chi^2$  value in the  $S_0$  experiment as a function of the Ramachandran angles ( $\Phi, \Psi$ ). (b) Cross section of the  $\chi^2$  function along the  $r_{C(Y34)-N(Y38)}$  parameter showing the data are best fit by simulations using a value of 4 Å. (c) The contour plot of the  $\chi^2(r_{C(P33)-N(Y38)}, \alpha)$  function along the minimum of the function at  $r_{C(Y34)-N(Y38)} = 4$  Å. (d) Cross section of the  $\chi^2$  function along the  $r_{C'-F(P23)}$  parameter showing the data are best fit by simulations using a value of 9 Å. (e) The contour plot of the  $\chi^2(r_{C'-F(P23)}, \alpha)$  function along the minimum of the function at  $r_{C'-F(P23)} = 9$  Å. Here, we denote the two carbons as C' and C'' since they are indistinguishable in the  $^{13}\text{C}$  spectrum. Confidence level of  $1 * \sigma$  is shown as the lowest contour in (a), (c), and (e) and the solid black line in (b) and (d).

where A sites dominate, and even below this temperature for any coverage above  $\sim 10\%$  of saturation. Adsorption of proteins to surfaces is often entropy driven and, in particular, the adsorption of two other salivary proteins PRP1 and PRP3 onto HAP.<sup>64</sup> The increase in entropy upon statherin adsorption is attributed to displacement of water molecules from the surface of the mineral and the solvation layer in the protein to solution.

We proposed that, at higher coverage, hydrophobic interactions are formed between coadsorbed protein molecules upon adsorption.<sup>6</sup> Also consistent with the data is that such interactions are usually characterized by high entropy due to the release of bound water to the solution.<sup>78,79</sup> The enthalpy of such interactions is composed of the enthalpy of packing of hydrophobic residues and the dehydration enthalpies of different residues. These two enthalpies are expected to have

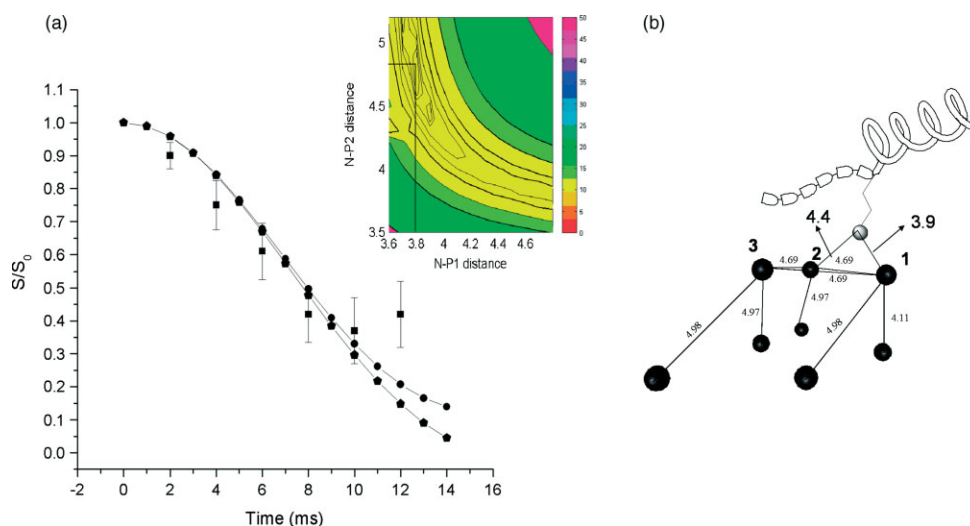


**Figure 9.** (a) Statistical  $\chi^2$  analysis of  $^{15}\text{N}$ – $^{31}\text{P}$  REDOR data of  $^{15}\text{N}$  K6 in SN15 to HAP indicates a well-defined minimum at distances of 3.8 and 4.8 Å, suggesting a possible hydrogen bond between the K6 side chain and the HAP atoms.<sup>53</sup> The filled squares are the experimental data, while the filled circles denote the simulation that gives rise to the  $\chi^2$  minimum and the pentagons indicate the multiple spin simulation of a  $^{15}\text{N}$  K6 approaching the (004) crystal plane of hydroxyapatite (parameters used for the simulation are defined thoroughly in (b)). (b) Model of a  $^{15}\text{N}$  K6 side chain of SN15 approaching the (004) crystal plane of hydroxyapatite. The figure depicts all the spins that were used in the above-mentioned simulation. The dark circles denote the  $^{31}\text{P}$  spins, while the lighter shaded circle depicts the  $^{15}\text{N}$  spin on the lysine side chain. The blocks on the peptide depict the six acidic *N*-terminal residues of SN15.

opposite signs,<sup>80</sup> which could explain the approximately zero enthalpy observed for the B-site-binding regime.

The temperature dependence of the adsorption thermodynamics determined from ITC shows that the change in the enthalpy upon adsorption to site A becomes less exothermic with increased temperature (Fig. 11, Table 1). The change in enthalpy with temperature resulted in a positive  $\Delta C_p$  value of  $194(\pm 7)$  cal  $\text{K}^{-1} \text{mol}^{-1}$  at 25 °C (Table 3 in Ref. 6). This *positive*  $\Delta C_p$  together with the observed *positive*  $\Delta S$  is inconsistent with this interaction being dominated by hydrophobic interactions common to protein–protein and protein–ligand interactions.<sup>81,82</sup> It is therefore reasonable that the positive  $\Delta C_p$  value observed here reflects an electrostatic interaction likely between the charged *N*-terminus of statherin and the ionic HAP surface sites.

We describe now the findings we obtained from the structural studies using NMR techniques and discuss in the following views and lessons to adsorption and functions of statherin that can be gained from the macroscopic and atomic level studies.

The dipolar recoupling measurements described in Sections on ‘Backbone structure of the *N*-terminal HAP binding domain’, ‘Secondary structure of the *C*-terminal bacterial binding domain’, and ‘Tertiary constraints on statherin fold’ were used in conjunction with the ROSETTA structure prediction algorithm to construct the folding of the mineral-bound protein. Refinement of the statherin structure was done by constraining the original 1000 model set with the long CF distance measurements and the geometric measurements in the *C*-terminus. The resultant eight structures, aligned along the backbone atoms in the two helices, are given in Fig. 11. They exhibit an average pair root-mean-square deviation (RMSD) of 2.5 Å with

higher structural dispersion in the intermediate region where constraints have not yet been measured. The small folded core is created by the folding of the *C*-terminus helical region (33–38) back onto the intermediate region through a loop region defined by proline residues. The *C*-terminus helix can be tilted at different angles with respect to the *N*-terminus helix due to the limited number of constraints between the two regions. The resultant torsion angle and distance values are not 1 : 1 correlated with maxima in the calculated values in the histograms of Fig. 6 (e.g.  $\phi$  angle). Only a single model out of the eight is common to the 31-model cluster used for labeling selection underscoring the predisposition that the predicted structure serves as a guideline for selection of label sites. The ROSETTA program thus successfully narrowed the search for structural elements in the folded protein and then enabled a construction of the protein fold based on the experimental distance constraints.

The view of the structure of surface-bound statherin that emerges from NMR measurements and structural modeling by ROSETTA is that of a protein with an  $\alpha$ -helical secondary structure encompassing the first 12 amino acids in the *N*-terminus. This region is known to be necessary for HAP binding and, accordingly,  $^{15}\text{N}$ – $^{31}\text{P}$  and  $^{13}\text{C}$ – $^{31}\text{P}$  REDOR measurements detected close approaches between surface phosphate groups and side chains of basic and aromatic amino acids. In addition, the *C*-terminus (which is known to contain a binding site for bacterial antenna proteins) is also helically structured. Long-distance  $^{13}\text{C}$ – $^{19}\text{F}$  measurements show that, unlike the condition in solution where statherin appears unfolded and displays a  $3_{10}$  helical structure near the *C*-terminus, on the mineral surface the *C*-terminal  $\alpha$  helix is folded over the intermediate region of the protein.

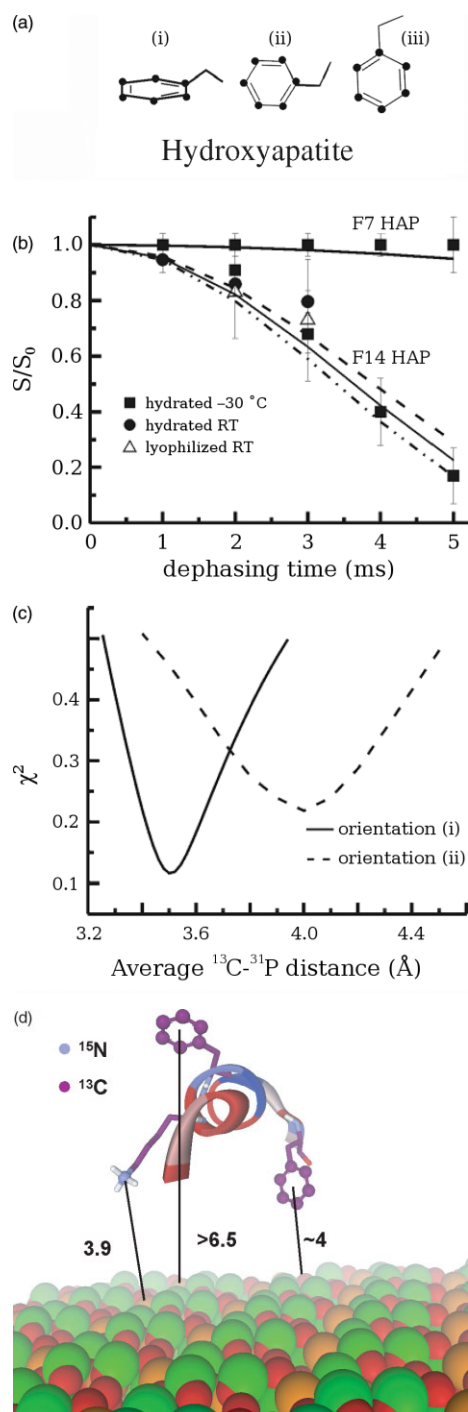


**Figure 10.** (a) Three different orientations of the phenyl ring with respect to the HAP surface were considered: (i) the ring plane is parallel to the HAP surface, (ii) the ring plane is perpendicular to the HAP surface with one meta- and one ortho- carbon closest to the surface, and (iii) the ring plane is perpendicular to the HAP surface with the para- carbon closest to the surface. (b) REDOR analysis of both the samples bound to HAP is shown. The experimental data and best simulated fits are shown for both samples. (c) A  $\chi^2$  map is shown for the F14 sample, based on the orientations (i) and (ii) depicted in Fig. 10(a). (d) A modified SN15 model with peptide bound to HAP is presented, in which the C-terminus loses its  $\alpha$ -helicity, and both the K6 and F14 side chains are within close proximity of the HAP surface<sup>54</sup>.

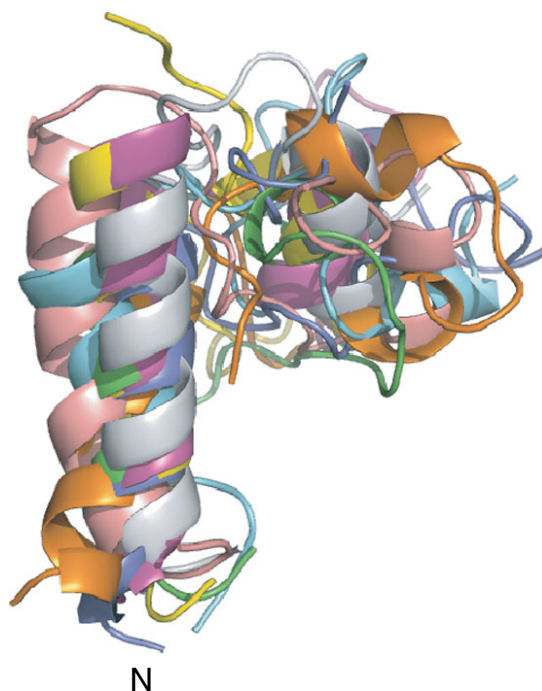


**Figure 11.** Superposition of the eight models that agree with the constraints derived from the solid-state NMR measurements.<sup>71</sup> These models are derived from the full set of 1000 models. Alignment of the models in the figure was based on the root-mean-square deviation calculation of segments (1–15) and (33–38) between the eight models. The N-terminus of the protein is denoted in the figure.

The next stage toward obtaining a detailed structure of the protein and its preferred orientation on the surface of HAP is to complement additional constraints on the structure and additional information regarding the proximity and hence interaction strength of the protein outer shell with a simulative effort that accounts for the potential energy that the protein encounters at the different faces of the mineral as it adsorbs.<sup>83</sup> The degree to which the structure of statherin can be influenced by the surface potential is not known yet, although for other proteins it was reported that changes as severe as total unfolding, especially on hydrophobic surfaces, are often observed. Current protein structure prediction programs cannot predict the folded state of a protein in the presence of another macromolecule or surface starting from an unfolded or random coil conformation. The ultimate goal of computational technique development would be to assert the experimental observation of a transition from an unfolded state to an active folded state upon exposure to the potential energy of the surface.<sup>83</sup>

## CONCLUSIONS

Isothermal titration microcalorimetry can detect even low heats involved in the adsorption of a protein to a mineral surface. It was successfully utilized to probe the thermodynamics of statherin adsorption onto HAP crystals. When analyzed in conjunction with results collected from AI, a clearer understanding of various adsorption mechanisms was achieved. At low coverage, statherin adsorbs onto

HAP with a significant favorable free energy change that is driven by both entropy and enthalpy. At higher coverage, the adsorption becomes enthalpically neutral and is driven solely by the positive entropy change associated with the release of bound water molecules. The higher affinity of the protein to the mineral at low coverage may be associated with adsorption to high energy surface sites like crystal growth sites and/or with a decreased affinity as a function of increased coverage due to unfavorable protein–protein interactions that lower the net free energy of adsorption. By blocking crystal growth sites first, statherin can inhibit HAP crystal growth at relatively low coverage as was previously reported.<sup>4,5</sup>

The NMR studies of HAP-bound statherin have given several insights with biological ramifications. Statherin binds to fimbriar systems in several bacterial microorganisms only when adsorbed onto HAP. The binding site for fimbriin, the monomeric unit of the fimbriae, is at the C-terminus of statherin. The conformational change in this region to an  $\alpha$ -helical motif upon adsorption as detected by solid-state NMR provides a clear avenue for the selective recognition of surface immobilized statherin by bacteria. The C-terminus of statherin has previously been associated with the lubricative action of statherin on tooth enamel. The helical motif at this region might have viscoelastic properties that help reduce wear of enamel surfaces. The lubricative action of statherin in concert with other proteins in the pellicle layer covering tooth surfaces should be greatly influenced by the structure that the protein adopts when adsorbed. Furthermore, if a cooperative mechanism of wear reduction between different proteins exists, recognition of statherin by different pellicle proteins requires that it adopts a stable structure in the pellicle.

The thermodynamic measurements showed that the spontaneous adsorption of statherin to the HAP surface has a positive entropy change as the dominant contribution for almost all the temperature range studied. The structural work implies reduction in the protein's motional degrees of freedom due to formation of secondary motifs and structuring of the protein upon adsorption. The increase in the degree of disorder upon binding of the protein to the surface of the mineral crystallites is therefore associated with the release of bound water around the outer surface of the protein and on the surfaces of the crystallites to allow for interaction between the two. The relatively low magnitude of the binding enthalpy,  $\sim 4$  kcal/mol, is not readily expected, given the number of charged residues in the protein at the working pH. Higher enthalpic contribution to the free energy might have been expected and this lower actual value may be important for the control of adsorption and desorption of the protein from the surfaces in response to functional needs and signals. The involvement of proton transfer in the adsorption process shown before<sup>6</sup> has a biological significance as well, given the fact that the saliva is exposed to major variations in pH. These studies provide a strong basis for future statherin structure–function studies and additional measurements that map the residues along the peptide chain that are involved in the interaction with mineral surface. Other important insights about the

function of the protein may be gained from studying the adsorbed complex of statherin with other tooth pellicle proteins as several studies have implied that these proteins form suprastructures on the enamel surface and may enhance their functionality by cooperative mechanism.

Statherin is a good model system whose structural transition upon adsorption to HAP crystallites provides leads for the structural basis for the function of biomineralization proteins. Many extracellular matrix proteins like osteopontin have segments in their primary sequence that are similar to statherin and have been found to be unstructured in solution.<sup>84</sup> In the case of statherin, the folding of the protein on the mineral surface may remove hydrophilic residues from solution, thus preventing further HAP nucleation. Previous studies have underscored the role of the C-terminus in retardation of HAP nucleation by statherin. The tertiary folding of statherin is the basis for its inhibition of both primary and secondary crystallization of HAP, and this folding is naturally induced by contact between the HAP surface and the protein. Thus, a protein that is unstructured in solution may nevertheless be functional on a surface where a folding transition occurs. This remarkable feature of statherin provides with a unique case of surface-induced structuring, which reverses the common paradigm observed in many proteins where surface-induced unfolding is observed.

### Acknowledgements

This work was supported by the NSF (Grants EEC 9529161 and DMR 0110505) and the NIH (National Dental Institute (RO1 DE-12554), and the Institute of General Medicine (RO1 GM074511)). We thank Dr Rajan Paranjani for his help in running the NMR experiments of statherin in solution and Dr Nicholas Breen for proof-reading the manuscript and for helpful discussions.

### REFERENCES

- Schoen FJ, Harasaki H, Kim KM, Anderson HC, Levy RJ. *J. Biomed. Mater. Res.* 1988; **22**: 11.
- Coe FL, Parks JH, Asplin JR. *N. Engl. J. Med.* 1992; **327**: 1141.
- McCarty DJ. *Dis. Mon.* 1994; **40**: 258.
- Raj PA, Johnsson M, Levine MJ, Nancollas GH. *J. Biol. Chem.* 1992; **267**: 5968.
- Johnsson M, Richardson CF, Bergey DJ, Levine MJ, Nancollas GH. *Arch. Oral Biol.* 1991; **36**: 631.
- Goobes R, Goobes G, Campbell CT, Stayton PS. *Biochemistry* 2006; **45**: 5576.
- Goobes R, Goobes G, Shaw WJ, Campbell CT, Drobny GP, Stayton PS. *Biochemistry* 2007; **46**: 4725.
- Sicheri F, Young DSC. *Nature* 1995; **375**: 427.
- Hoang QQ, Sicheri F, Howard AJ. *Nature* 2003; **425**: 977.
- Lee VA, Craig RG, Filisko FE, Zand R. *J. Colloid Interface Sci.* 2005; **288**: 6.
- Norde W, Lyklema J. *J. Colloid Interface Sci.* 1978; **66**: 257.
- Koutsoukos PG, Norde W, Lyklema J. *J. Colloid Interface Sci.* 1983; **95**: 385.
- Chiu TH, Nyilas E, Lederman DM. *Trans. Am. Soc. Artif. Intern. Organs* 1976; **22**: 498.
- Haynes CA, Norde W. *J. Colloid Interface Sci.* 1995; **169**: 313.
- Pan VH, Tao T, Zhou JW, Maciel GE. *J. Phys. Chem. B* 1999; **103**: 6930.
- Sindorf DW, Maciel GE. *J. Am. Chem. Soc.* 1983; **105**: 1848.
- Brunner E, Seydoux R, Haake M, Pines A, Reimer JA. *J. Magn. Reson.* 1998; **130**: 145.
- Wang P-K, Slichter CP. *Phys. Rev. Lett.* 1984; **53**: 82.
- Hwang S-J, Petucci C, Raftery D. *J. Am. Chem. Soc.* 1998; **120**: 4388.

20. Tong YY, Rice C, Wieckowski A, Oldfield E. *J. Am. Chem. Soc.* 2000; **122**: 11921.
21. Beshah K, Rey C, Glimcher MJ, Shimizu M, Griffin RG. *J. Magn. Reson.* 1990; **84**: 17.
22. Yesinowski JP. Nuclear magnetic resonance of calcium phosphates. In *Calcium Phosphates in Biological and Industrial Systems*, Amjad Z (ed). Kluwer Academic Publishers: Boston, 1988.
23. Wu Y, Ackerman JL, Strawich ES, Rey C, Kim HM, Glimcher MJ. *Calcif. Tissue Int.* 2003; **72**: 610.
24. Bak M, Thomsen JK, Jakobsen HJ, Petersen SE, Petersen TE, Nielsen NC. *J. Urol.* 2000; **164**: 856.
25. Denny JK, Wang JF, Cross TA, Quine JR. *Biophys. J.* 2001; **80**: 1555.
26. Castellani F, van Rossum B, Diehl A, Schubert M, Rehbein K, Oschkinat H. *Nature* 2002; **420**: 98.
27. Tycko R. *Prog. Nucl. Magn. Reson.* 2003; **42**: 53.
28. Drobny GP, Stayton PS, Long JR, Louie EA, Karlsson T, Popham JM, Oyler NA, Bower PV, Shaw WJ. Structural studies of peptides at biomaterial interfaces using double quantum solid state NMR spectroscopy. In *Biological Solid State NMR*, Ramamoorthy A (ed). Taylor & Francis: New York, 2005.
29. Goobes G, Stayton PS, Drobny GP. *Prog. Nucl. Magn. Reson. Spectrosc.* 2007; **50**: 71.
30. Gregory D, Mitchell D, Stringer JA, Kiihne S, Shiels JC, Callahan J, Mehta MA, Drobny GP. *Chem. Phys. Lett.* 1995; **246**: 654.
31. Gullion T, Schaefer J. *J. Magn. Reson.* 1989; **81**: 196.
32. Gullion T, Vega S. *Chem. Phys. Lett.* 1992; **194**: 423.
33. Bennet AE, Ok JH, Griffin RG, Vega S. *J. Chem. Phys.* 1992; **96**: 8624.
34. Schupbach P, Oppenheim FG, Lendenmann U, Lamkin MS, Yao Y, Guggenheim B. *Eur. J. Oral Sci.* 2001; **109**: 60.
35. Li J, Helmerhorst EJ, Yao Y, Nunn ME, Troxler RF, Oppenheim FG. *Arch. Oral Biol.* 2004; **49**: 379.
36. Vitkov L, Hannig M, Nekrashevych Y, Krautgartner WD. *Eur. J. Oral Sci.* 2004; **112**: 320.
37. Yin A, Margolis H, Yao Y, Grogan J, Oppenheim FG. *Arch. Oral Biol.* 2006; **51**: 102.
38. Douglas WH, Reeh ES, Ramasubbu N, Raj PA, Bhandary KK, Levine MJ. *Biochem. Biophys. Res. Commun.* 1991; **180**: 91.
39. Hahn Berg IC, Lindh L, Arnebrant T. *Biofouling* 2004; **20**: 65.
40. Proctor GB, Hamdan S, Carpenter SH, Wilde P. *Biochem. J.* 2005; **389**: 111.
41. Hay DI, Moreno EC. In *Human Saliva: Clinical Chemistry and Microbiology*, Vol. I, Tenovuo JO (ed). CRC Press: Boca Raton, 1989; 131.
42. Schlesinger DH, Hay DI. *J. Biol. Chem.* 1977; **252**: 1689.
43. Raj PA, Marcus E, Sukumaran DK. *Biopolymers* 1992; **45**: 51.
44. Schwartz SS, Hay DI, Schluckebier SK. *Calcif. Tissue Int.* 1992; **50**: 511.
45. Campbell AA, Ebrahimpour A, Perez L, Smesko SA, Nancollas GH. *Calcif. Tissue Int.* 1989; **45**: 122.
46. Jensen JL, Lamkin MS, Oppenheim FG. *J. Dent. Res.* 1992; **71**: 1569.
47. Johnsson M, Levine MJ, Nancollas GH. *Crit. Rev. Oral Biol. Med.* 1993; **4**: 371.
48. Moreno EC, Kresak M, Hay DI. *Arch. Oral Biol.* 1978; **23**: 525.
49. Waite JH, Qin X. *Biochemistry* 2001; **40**: 2887.
50. Aoba T, Moreno EC, Hay DI. *Calcif. Tissue Int.* 1984; **36**: 651.
51. Wikiel K, Burke EM, Perich JW, Reynolds EC, Nancollas GH. *Arch. Oral Biol.* 1994; **39**: 715.
52. Gibson JM, Raghunathan V, Popham JM, Stayton PS, Drobny GP. *J. Am. Chem. Soc.* 2005; **127**: 9350.
53. Raghunathan V, Gibson JM, Goobes G, Popham JM, Louie AE, Stayton PS, Drobny GP. *J. Phys. Chem. B* 2006; **110**: 9324.
54. Gibson JM, Popham JM, Raghunathan V, Stayton PS, Drobny GP. *J. Am. Chem. Soc.* 2006; **128**: 5364.
55. Lamont RJ, Jenkinson HF. *Microbiol. Mol. Biol. Rev.* 1998; **62**: 1244.
56. Dodds MWJ, Johnson DA, Yeh C-K. *J. Dent.* 2005; **33**: 223.
57. Rudney JD, Chen R. *Arch. Oral Biol.* 2004; **49**: 523.
58. Gibbons RJ, Hay DI. *Infect. Immun.* 1988; **56**: 439.
59. Gibbons RJ, Hay DI, Schlesinger DH. *Infect. Immun.* 1991; **59**: 2948.
60. Xie H, Gibbons R, Hay D. *Oral Microbiol. Immunol.* 1991; **6**: 257.
61. Amano A, Kataoka K, Raj PA, Genco RJ, Shizukuishi S. *Infect. Immun.* 1996; **64**: 4249.
62. Nagata H, Sharma A, Sojar HT, Amano A, Levine MJ, Genco RJ. *Infect. Immun.* 1997; **65**: 422.
63. Sekine S, Kataoka K, Tanaka M, Nagata H, Kawakami T, Akaji K, Aimoto S, Shizukuishi S. *Microbiology* 2004; **150**: 2373.
64. Moreno EC, Kresak M, Hay DI. *Calcif. Tissue Int.* 1984; **36**: 48.
65. Gray JJ. *Curr. Opin. Struct. Biol.* 2004; **14**: 110.
66. Mura-Galelli MJ, Voegel JC, Behr S, Bres EF, Schaaf P. *Proc. Natl. Acad. Sci.* 1991; **88**: 5557.
67. Ramsden JJ. *Chem. Soc. Rev.* 1995; **24**: 73.
68. Naganagowda GA, Gururaja TL, Levine MJ. *J. Biomol. Struct. Dyn.* 1998; **16**: 91.
69. Elgavish GA, Hay DI, Schlesinger DH. *Int. J. Pept. Protein Res.* 1984; **23**: 230.
70. Long JR, Shaw WJ, Stayton PS, Drobny GP. *Biochemistry* 2001; **40**: 15451.
71. Goobes G, Goobes R, Schueler-Furman O, Baker D, Stayton PS, Drobny GP. *Proc. Natl. Acad. Sci. U.S.A.* 2006; **103**: 16083.
72. Rohl CA, Strauss CEM, Misura KMS, Baker D. *Methods Enzymol.* 2004; **383**: 66.
73. Goobes G, Raghunathan V, Louie EA, Gibson JM, Olsen GL, Drobny GP. *Solid State Nucl. Magn. Reson.* 2006; **29**: 242.
74. Koutsopoulos S, Dalas E. *Langmuir* 2000; **16**: 6739.
75. Minton AP. *Biophys. J.* 1999; **76**: 176.
76. Sun Y, Welsh WJ, Latour RA. *Langmuir* 2005; **21**: 5616.
77. Norde W. *Adv. Colloid Interface Sci.* 1986; **25**: 267.
78. Robinson GW, Cho CH. *Biophys. J.* 1999; **77**: 3311.
79. Makhataдзе GM, Privalov PL. *J. Mol. Biol.* 1993; **232**: 660.
80. Makhataдзе GM, Privalov PL. *J. Mol. Biol.* 1993; **232**: 639.
81. Loladze VV, Ermolenko DN, Makhataдзе GI. *Protein Sci.* 2001; **10**: 1343.
82. Sturtevant JM. *Proc. Natl. Acad. Sci.* 1977; **74**: 2236.
83. Makrodimitris K, Masica DL, Kim ET, Gray JJ. *J. Am. Chem. Soc.* 2007; **129**: 13713.
84. Fisher LW, Torchia DA, Fohr B, Young MF, Fedarko NS. *Biochem. Biophys. Res. Commun.* 2001; **280**: 465.